Powder Technology 478 (2026) 122520

Contents lists available at ScienceDirect

Powder Technology

journal homepage: www.journals.elsevier.com/powder-technology

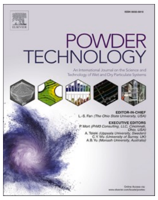

Influence of particle size distribution and contact models on tablet compaction: A DEM micromechanical study

Amine Ait Ouazzou [a,*], Yogesh M. Harshe [b], Vincent Meunier [b], Jan H. Finke [c], Stefan Heinrich [a]

[a] *Institute of Solids Process Engineering and Particle Technology, Hamburg University of Technology, Hamburg, Germany*
[b] *Nestlé Research, Route du Jorat 57, Lausanne 1000, Switzerland*
[c] *Institute for Particle Technology and Center of Pharmaceutical Engineering - PVZ, Technical University of Braunschweig, Germany*

HIGHLIGHTS

- Broader PSDs yield higher final density and lower elastic recovery in DEM compaction.
- PSD broadening increases connectivity and shifts force transmission by particle size.
- Hertz Mindlin JKR and EEPA load similarly but diverge strongly during unloading.
- EEPA retains plastic overlap, yielding denser compacts and more persistent contacts.
- PSD design and contact model choice jointly control predicted tablet microstructure.

GRAPHICAL ABSTRACT

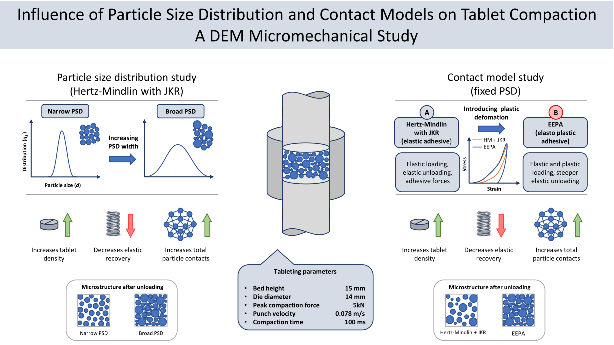

- Bed height 15 mm
- Die diameter 14 mm
- Peak compaction force 5kN
- Punch velocity 0.078 m/s
- Compaction time 100 ms

ARTICLE INFO

Keywords:
Tablet compaction
Discrete element method
Particle size distribution
Hertz–Mindlin–JKR
Edinburgh Elasto-plastic adhesion (EEPA)

ABSTRACT

The tableting process relies on understanding how particle-scale properties influence macroscopic tablet behaviour. This study examines the effects of particle size distribution (PSD) and contact models on tablet compaction using the Discrete Element Method (DEM). The PSD analysis shows that broader distributions achieve higher final densities and reduced elastic recovery. To assess the impact of contact mechanics, two cohesive DEM models, Hertz–Mindlin with Johnson–Kendall–Roberts (JKR) adhesion and the Edinburgh Elasto-Plastic Adhesion (EEPA) model, were compared under identical compaction kinematics. While both models follow similar loading behaviour, the EEPA formulation retains more of the imposed deformation during unloading, resulting in higher final densities, lower elastic recovery, and a more persistent contact structure than the elastic–adhesive Hertz–Mindlin–JKR model. These results emphasise the importance of both PSD design and contact-model selection when predicting compaction behaviour and final tablet structure in DEM-based analysis of cohesive powders.

---

[*] Corresponding author.
E-mail address: amine.ait.ouazzou@tuhh.de (A. Ait Ouazzou).

https://doi.org/10.1016/j.powtec.2026.122520
Received 16 February 2026; Received in revised form 31 March 2026; Accepted 3 April 2026

Table of symbols

Latin symbols

F_n	Normal contact force; [N]
F_t	Tangential contact force; [N]
F_{JKR}	Total normal contact force of JKR; [N]
F_{hys}	Hysteretic spring force; [N]
F_{nd}	Normal damping force; [N]
F_0	Constant adhesive force; [N]
k_1	Loading stiffness parameters; [N/m]
k_2	Unloading stiffness parameters; [N/m]
k_{adh}	Adhesive stiffness parameters; [N/m]
R^*	Equivalent radius of the particles; [m]
E^*	Equivalent Young's modulus of the particles; [Pa]
S_t	Tangential stiffness; [N/m]
n	Non-linear index parameter; [−]
a	Contact radius; [m]
ν_n	Magnitude of relative normal velocity; [m/s]
β_n	Normal dashpot co-efficient; [−]

Greek letters

δ	Normal overlap between the particles; [m]
δ_T	Tangential overlap between the particles; [m]
δ_p	Plastic particle overlap; [m]
γ	Surface energy; [J/m^2]

Abbreviations

PSD	Particle size distribution
PDF	Probability density function

1. Introduction

1.1. The significance of the tableting process

The tableting process is crucial across several industrial sectors due to its central role in producing uniform and precise solid products. It is especially dominant in pharmaceutical manufacturing, where direct compression and related processes remain central to modern continuous manufacturing and digital process-modelling strategies [1–4].

In the pharmaceutical industry, tablets are the preferred dosage form due to their ease of administration, high stability, long shelf-life, and cost-efficient manufacturing. These characteristics remain central even in advanced manufacturing environments such as continuous direct compression, where tablet properties are tightly linked to material behaviour, compaction mechanics and process control [3,5,6].

In the food and nutraceutical sectors, tableting enables the production of compact solid forms such as stock cubes and dietary supplements. The process improves handling, storage stability and dosage control while maintaining nutritional integrity [4,7,8]. Recent developments in consumer health products and functional foods have further increased the demand for consistent, tabletised formats [4].

The tableting process involves several critical stages including blending, granulation, drying, compression and coating [4,9,10]. Among these, compression is a crucial stage, as it transforms powder or granular materials into a compact solid dosage form under compressive forces. The efficiency of the manufacturing process and the quality of the final product are significantly influenced by various factors, including raw material properties, equipment design, and process parameters, each impacting the final product's properties differently.

1.2. The role of particle size distribution in tableting

The particle size distribution (PSD) strongly influences several critical quality attributes of a tablet. It determines bulk flowability and cohesiveness, which directly govern die filling, dosing reliability and process robustness [11–13].

Flowability is particularly sensitive to PSD because it dictates how easily a powder fills the die cavity, thereby influencing weight variation between tablets. Powders with favourable flow characteristics support more uniform filling and increase the consistency of tablet mass and content [14].

PSD also shapes the mechanical and functional properties of the final tablet. Particle size affects compressibility, compactibility, hardness, friability, disintegration behaviour, and even dissolution performance [12,15]. Smaller particles typically show higher surface-area-to-volume ratios and form more interparticle contacts during compression, which enhances compactibility and promotes stronger bonding [16–18]. Recent micromechanical analyses further demonstrate that PSD controls how force chains develop during densification and how stress is redistributed across fines and coarse fractions [17,18].

Beyond the mean particle size, the width of the PSD plays an equally critical role. Narrow PSDs promote reproducible flow and robust die filling, while broader PSDs improve packing efficiency by allowing smaller particles to occupy voids between larger ones [18,19]. Recent studies show that multimodal and bimodal mixtures develop more heterogeneous but mechanically favourable contact networks, resulting in higher densification under load [18].

Overall, controlling PSD is essential for balancing manufacturability with tablet performance. Both our study and recent work [13,16–18] indicate that these effects originate from particle-scale interactions, bond density evolution and the restructuring of force networks during compression. The role of PSD will be revisited in the Discussion, where the simulation results are compared with these micromechanical trends.

1.3. Maltodextrin

Maltodextrin is a widely used polysaccharide produced through the partial hydrolysis of starch, consisting primarily of α-(1,4) and α-(1,6) linked glucose units. Its physicochemical properties depend strongly on its degree of polymerisation and dextrose equivalent, which govern solubility, film-forming behaviour and its performance as a carrier or excipient [20–23].

In pharmaceutical formulations, maltodextrin is widely employed as a filler and binder due to its high solubility, non-reactive nature and favourable compaction behaviour. It also functions as a carrier or stabilising agent in spray-dried systems and as a coating or matrix former in controlled-release applications [20,21]. Recent studies confirm its continued relevance as a versatile excipient in solid and semi-solid dosage forms [21–23].

In the food and nutraceutical sectors, maltodextrin is a standard carrier, bulking agent and encapsulation matrix used in spray drying and freeze drying of plant extracts, vitamins and flavours. It improves powder flow, stability and reconstitution behaviour, and is frequently incorporated into dietary supplements and functional foods [21–24].

1.4. DEM in tablet manufacturing

Discrete Element Modelling (DEM) is a particle-scale simulation technique widely applied to granular flow, powder processing and compaction problems. By modelling individual particles and their interactions, DEM provides access to micromechanical quantities such as force chains, contact evolution and local densification that are not directly measurable experimentally [25–27]. Recent studies demonstrate that DEM can reliably reproduce packing evolution, stress transmission and pore-structure changes during tablet compaction when contact models and material parameters are appropriately calibrated [27–29].

In tablet manufacturing, DEM has been used extensively to analyse powder compaction, enabling the study of load distribution, interparticle bonding and structural evolution throughout the compression–unloading cycle [30,31]. Modern DEM approaches also link microstructure to tablet-level properties such as density, tensile strength and disintegration, making DEM a valuable tool for formulation and process design [27–29].

Several contact-force models exist in DEM, each capturing different aspects of particle deformation, adhesion and energy dissipation. The choice of contact model strongly influences predicted densification, force transmission, elastic recovery and residual microstructure [28,29,32–34]. Adhesive and elastoplastic contact formulations have recently been shown to be particularly important for cohesive and amorphous powders such as maltodextrin, where irreversible deformation and bonding dominate the compaction behaviour [28,29].

In this study, we investigate how systematic variations in particle size distribution, and separately the use of different adhesive contact models for a fixed PSD, influence the tableting behaviour of maltodextrin. We focus on key descriptors of compaction such as interparticle force transmission, tablet density, and elastic recovery. While experimental measurements provide a basis for the initial calibration, the aim of this work is not to reproduce exact experimental curves. Instead, we seek to identify the underlying trends and physical mechanisms that emerge during compaction. The simulations are therefore intended to capture the general behaviour of the system and highlight how PSD and contact-model assumptions shape the resulting tablet structure, rather than to provide absolute numerical predictions.

2. Materials and methods

2.1. Materials properties and characterisation

The material chosen for this study is maltodextrin in the form of dried glucose syrup at a dextrose equivalent level of 29 under the brand name Glucidex 29IT from Roquette Frères (Lestrem, France) referred to as 29IT in this study, a commonly used excipient and filler in the pharmaceutical [20] and food industries [35].

2.1.1. Particle morphology

Particle morphology was investigated by means of scanning electron microscopy (Helios G4 CX, Thermo Fisher Scientifc, USA) as shown in Fig. 1. The samples were sputtered with gold (LEICA EM ACE600, Leica microsystems GmbH, Germany) prior to measurements.

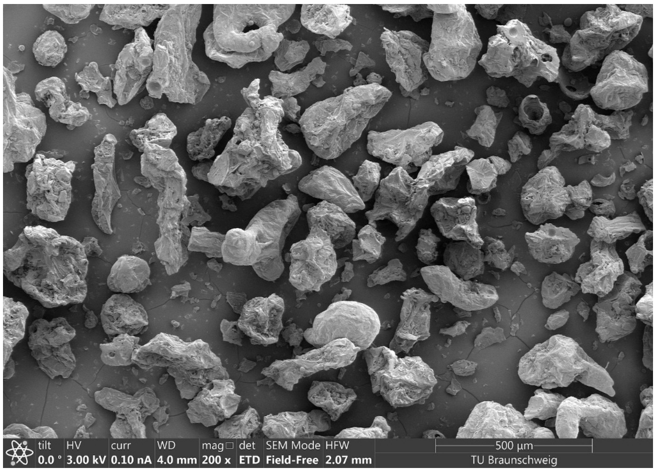

Fig. 1. Scanning electron microscopy (SEM) image of glucidex 29IT maltodextrin.

The particles in Fig. 1 exhibit an irregular, agglomerated morphology with rounded edges and a broad size range, typical of spray-dried maltodextrin. Individual particles appear smooth, while larger agglomerates show a more porous surface structure. Such morphologies are typical of spray-dried carbohydrate powders and strongly influence packing and deformation behaviour [22,27].

In the DEM simulations, however, particles were represented as spheres in order to maintain computational tractability and to isolate the effects of PSD breadth and contact law within a controlled framework. The objective of the present study is therefore not to reproduce the exact particle geometry, but to compare the relative micromechanical trends associated with PSD and contact model choice. To partially compensate for this simplification at the bulk level, an effective particle density was calibrated to reproduce a realistic die filling state.

2.1.2. Particle size distribution

The particle size distribution (PSD) of maltodextrin Fig. 2 was measured using a CAMSIZER XT dynamic image analysis system (Retsch GmbH, Germany). A dispersion pressure of 50 kPa was applied to minimize agglomerate breakage while ensuring reliable detection of individual particles. The resulting cumulative PSD served as the basis for constructing discrete size classes for the DEM simulations.

To construct these classes, the experimental PSD was translated into ten representative particle diameters. The central size class was selected near the mode of the distribution (402 µm), and additional classes were added progressively by alternating toward smaller and larger diameters. This “center-outward” selection ensures that the full range of the measured PSD is covered while preserving the relative spacing between characteristic sizes. The resulting ten size classes (101, 227, 280, 323, 362, 402, 446, 498, 571 and 683 µm) provide a balanced and physically meaningful representation of the PSD for subsequent DEM analysis. This approach avoids over-emphasizing the distribution tails and retains the characteristic shape of the experimental PSD more effectively than percentile-based boundaries. The percentage contribution of each class shown in Table 1 corresponds to its mass fraction, ensuring that all PSDs contain the same total powder mass.

For computational efficiency, all particle diameters were uniformly scaled by a factor of three. This reduces the total number of particles while maintaining the relative proportions between size classes. A single scaling factor was applied throughout the study to ensure consistent calibration and avoid re-tuning material or contact parameters for different particle sizes. The final scaled size classes are shown in Table 1, with Fig. 3 illustrating their distribution and Fig. 4 reporting the corresponding particle counts for each class.

Although geometric scaling alters absolute particle dimensions, uniform scaling preserves the relative PSD shape and associated packing behaviour [32,36]. Such uniform geometric scaling is widely used in

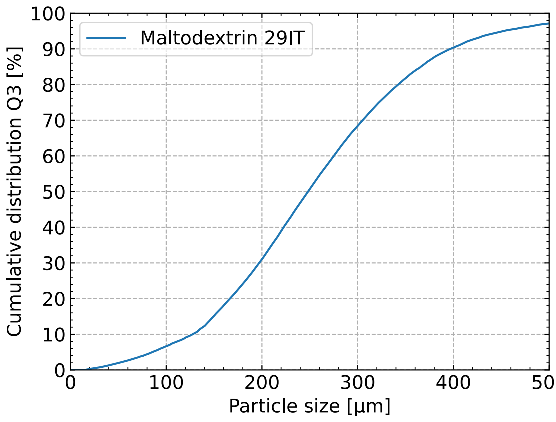

Fig. 2. Cumulative particle size distribution for maltodextrin Glucidex 29IT.

Table 1
PSDs scaled by a factor of 3.

	Size Classes [µm]										
PSD	101	227	280	323	362	402	446	498	571	683	Total N° of particles
1	0%	0%	0%	0%	0%	100%	0%	0%	0%	0%	3470
2	0%	0%	0%	0%	50%	50%	0%	0%	0%	0%	4103
3	0%	0%	0%	33.33%	33.33%	33.33%	0%	0%	0%	0%	4968
4	0%	0%	0%	25%	25%	25%	25%	0%	0%	0%	4359
5	0%	0%	0%	20%	20%	20%	20%	20%	0%	0%	3851
6	0%	0%	0%	16.66%	16.66%	16.66%	16.66%	16.66%	0%	0%	4905
7	0%	0%	0%	14.29%	14.29%	14.29%	14.29%	14.29%	14.29%	0%	4376
8	0%	12.5%	12.5%	12.5%	12.5%	12.5%	12.5%	12.5%	12.5%	0%	6216
9	0%	11.11%	11.11%	11.11%	11.11%	11.11%	11.11%	11.11%	11.11%	11.11%	5601
10	10%	10%	10%	10%	10%	10%	10%	10%	10%	10%	26,632

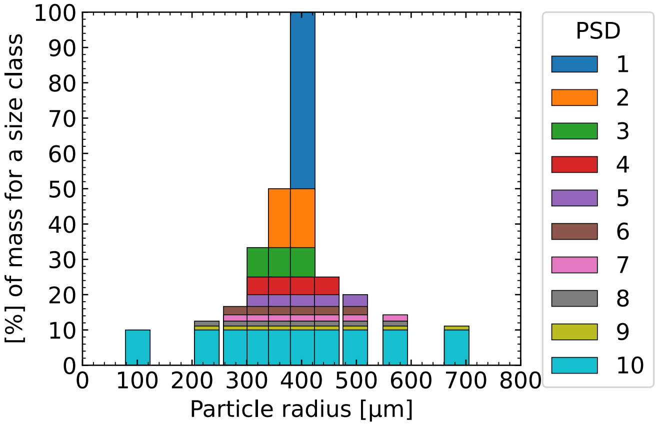

Fig. 3. Bar chart of size-class percentages for all PSDs 1–10 after applying a uniform scaling factor of 3.

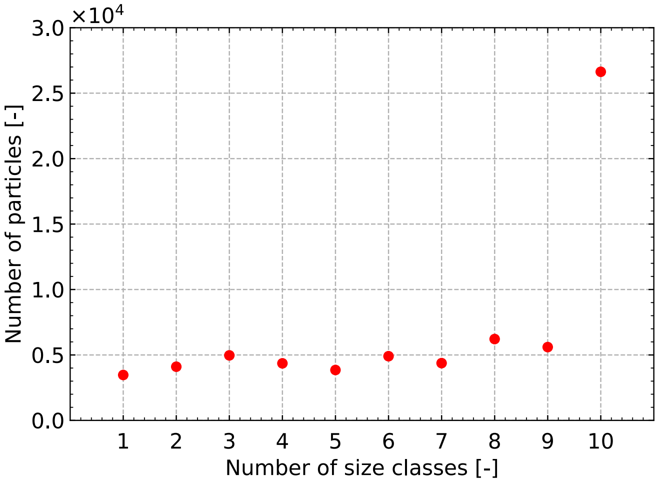

Fig. 4. Particle count by PSD size class.

DEM studies of cohesive powders to reduce computational cost while maintaining representative packing, coordination and force transmission, provided material parameters are calibrated for the scaled system [36,37].

Because each PSD contains the same total mass of powder, the number of particles in each distribution depends directly on the sizes represented in it. Adding a larger size class reduces the total particle count, since one large particle replaces many smaller ones of equivalent mass. Conversely, introducing a smaller size class produces a sharp increase in particle number, as a fixed mass corresponds to a much larger number of small particles. Since the PSD sets 1–10 were constructed by alternating the addition of smaller and larger classes, the total number of particles evolves in a non-monotonic, oscillating manner rather than gradually increasing. This effect becomes most pronounced in PSD 10, where the smallest size classes are present and the number of particles is substantially higher than in the narrower PSDs.

2.1.3. Particle density

The simulations incorporated a particle density of 1300 kg/m^3, a value approximating the real-world density of 1550 kg/m^3 measured with a helium pycnometer (Accupyc II 1340, Micromeritics, United States) [38]. This reduced value represents an effective density used to compensate for the spherical particle approximation in DEM. It is introduced during calibration to ensure that the simulated bulk density after die filling matches the experimentally observed fill height.

The particle density used in DEM should therefore be interpreted as an effective material parameter chosen to reproduce the experimentally measured bulk density rather than the true solid density of maltodextrin.

2.1.4. Micro-indentation

Micromechanical compression tests were carried out on individual maltodextrin particles using a Hysitron TI 950 triboindenter equipped with a flat punch of 500 µm diameter. No formal indentation strain rate was defined in the original test protocol, as the measurements were intended only for qualitative assessment of particle scale deformation behaviour. A total of 42 load displacement curves were recorded from 42 separate particles. This number was selected according to the standard experimental acquisition protocol and was considered sufficient to capture particle to particle variability in the local response. All tests showed monotonic loading with displacement depths of roughly 2 to 3 µm under loads approaching 1.5 N. However, none of the curves exhibited a distinct elastic unloading segment, and the overall response was strongly nonlinear. Representative load displacement curves are shown in Fig. 6, while Fig. 5 shows a maltodextrin particle before and after micro indentation testing. The absence of a measurable unloading branch indicates that the particles deform through extensive plastic flow and interfacial adhesion rather than recoverable elasticity.

This behaviour is consistent with the mechanics of soft amorphous materials exhibiting viscoelastic, viscoplastic, and adhesive deformation, in which pronounced time dependence and energy dissipation may occur during indentation, with only a limited fraction of the work stored elastically. [39–41]. In such systems, the classical Oliver–Pharr analysis requires a clearly defined elastic unloading slope and is not appropriate when the unloading response is dominated by viscoplasticity and adhesion.

For this reason, the indentation data in this study were used only qualitatively to confirm the deformable and adhesive character of the maltodextrin particles and to provide physical support for the use of an effective DEM calibration strategy, rather than for direct extraction of elastic constants or direct transfer of intrinsic parameters into the contact law. Instead, the DEM simulations employed an effective Young modulus of 1 GPa and a Poisson ratio of 0.25. These values fall within

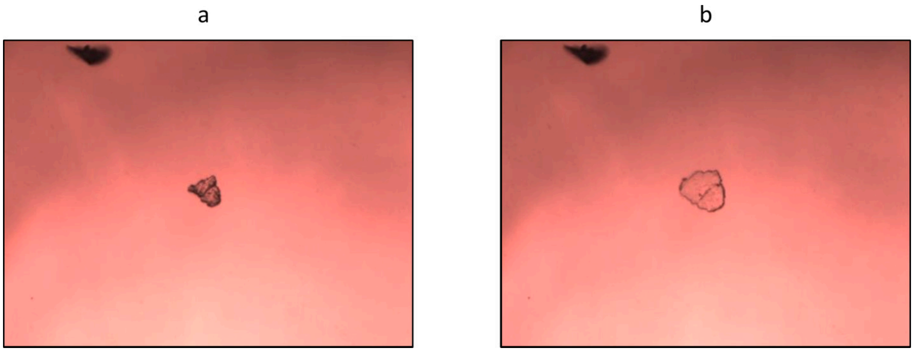

Fig. 5. Images of maltodextrin particle before (a) and after (b) micro-indentation testing.

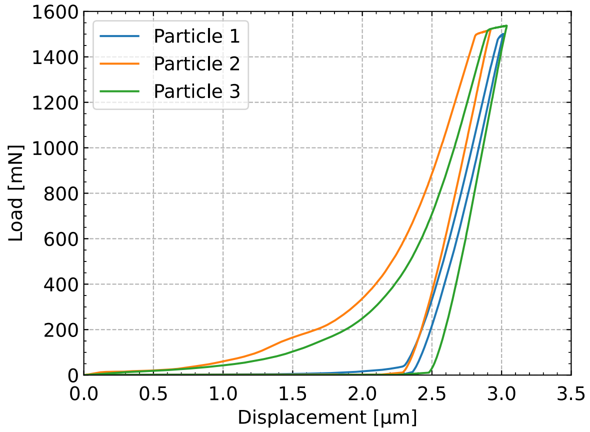

Fig. 6. Representative load–displacement curves obtained by micro-indentation for three individual maltodextrin particles.

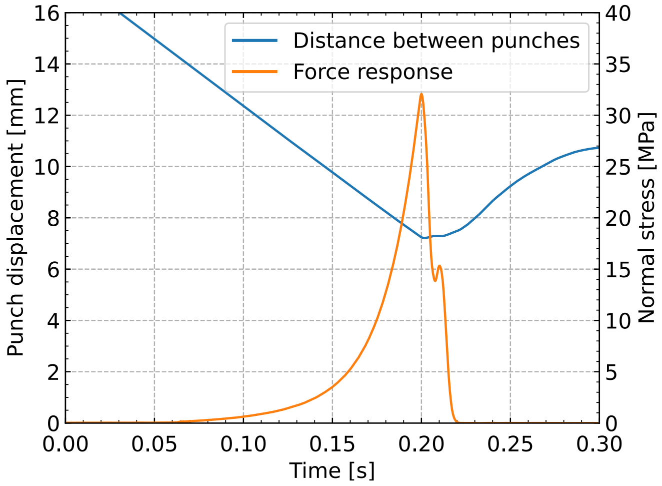

Fig. 7. STYL'One Evo compaction profile showing punch displacement and force response during a 5 kN peak compaction force and 1 ms dwell-time experiment.

the range commonly used in DEM simulations of cohesive powders and represent calibrated particle scale stiffness parameters rather than the true bulk modulus of the material [31,32,36,37].

Recent calibration studies for cohesive and fine materials emphasise that effective elastic parameters should be selected so that the DEM model reproduces macroscopic bulk behaviour, within a chosen contact law, rather than attempting to match intrinsic material moduli one to one [31,32,37]. In this sense, the strongly nonlinear indentation response and the absence of a distinct elastic unloading branch provide qualitative support for considering an elastoplastic adhesive description such as EEPA in the present DEM analysis, although the indentation data were not used here to uniquely identify the contact law or its parameters. In the present work, the effective modulus and effective particle density were therefore chosen during calibration to match the experimentally measured die fill bulk density and the force displacement response of the compaction simulator, providing a consistent contact stiffness for the subsequent particle size distribution and contact model investigations [32,42,43].

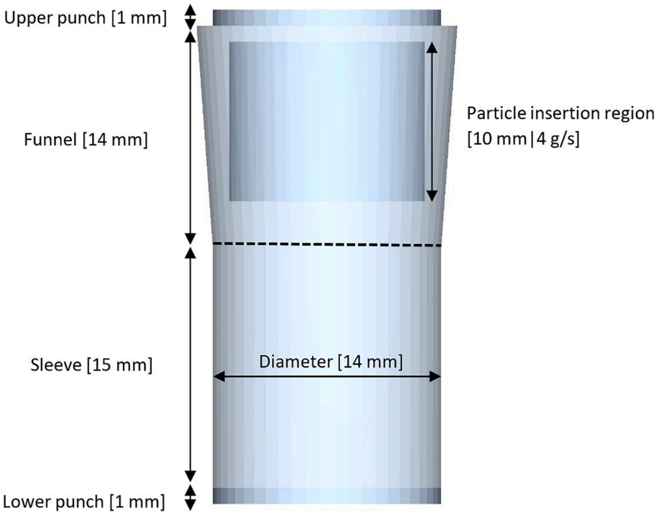

Fig. 8. Schematic of the DEM simulation setup, showing the cylindrical die, upper and lower punches, sleeve, and particle insertion region

2.1.5. *Mixing and tableting*

The tableting experiments were conducted on a STYL'One Evo compaction simulator (Medel'Pharm, France). To reduce die–wall friction, sodium stearyl fumarate (PRUV®, JRS Pharma, Germany) was incorporated at 0.5% *w*/w into a 250 g batch of maltodextrin. The blend was mixed for 2 min using a Turbula T2F mixer at 49 rpm. This mixing duration was selected to ensure homogeneous lubricant distribution while avoiding excessive over-mixing, which is known to reduce tabletability and affect bonding in plastifying excipients [9,16].

The tooling consisted of biplanar punches and a cylindrical die with a diameter of 14 mm. The die was filled to an initial powder height of 15 mm. The punches followed a linear displacement profile until a peak compaction force of 5 kN was reached, consistent with typical instrumented compaction protocols used for formulation screening [3,4]. Fig. 7 shows a punch displacement and force response curves from the STYL'One Evo under these settings.

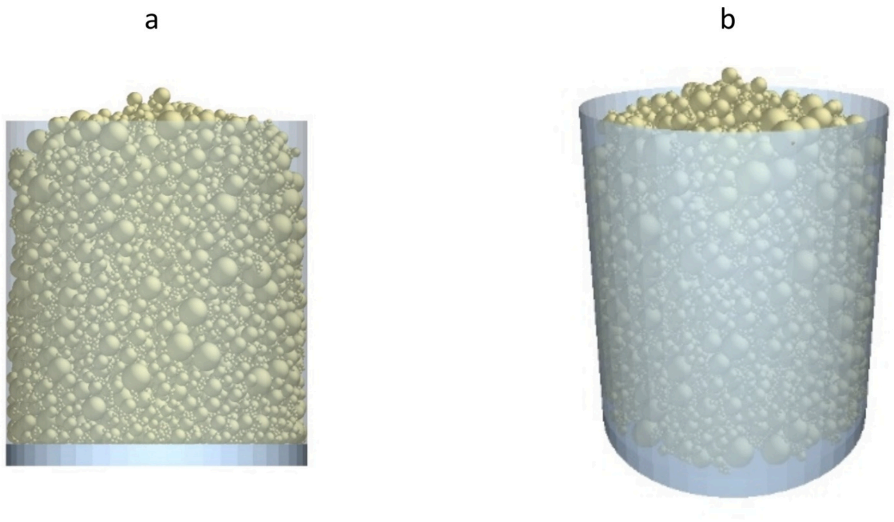

Fig. 9. Side (a) and inclined (b) views of the powder-filled compaction die used for bulk-density calibration.

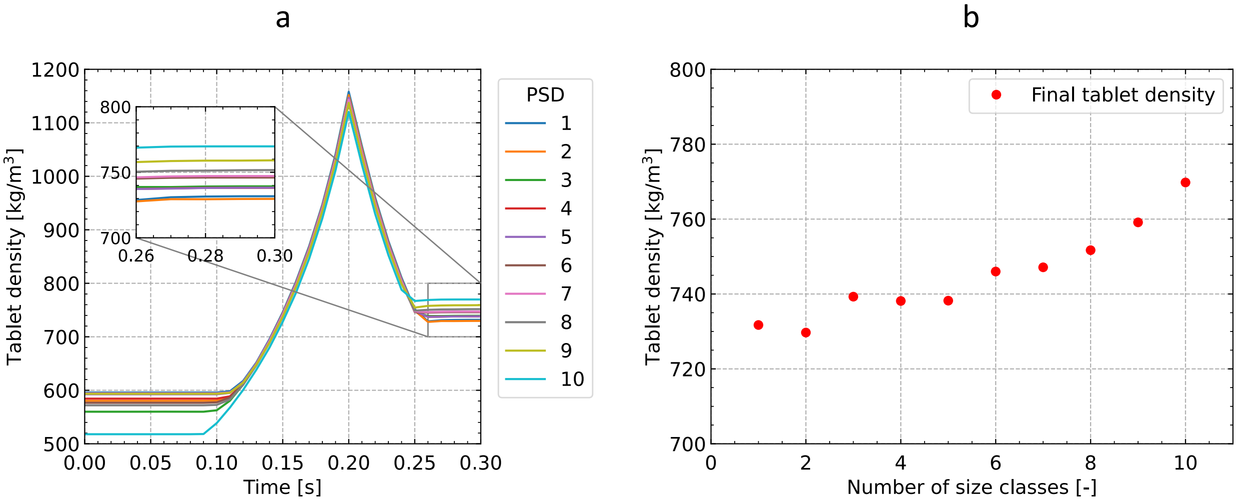

Fig. 10. Tablet density evolution for all ten PSDs: temporal evolution (a), final densities (b).

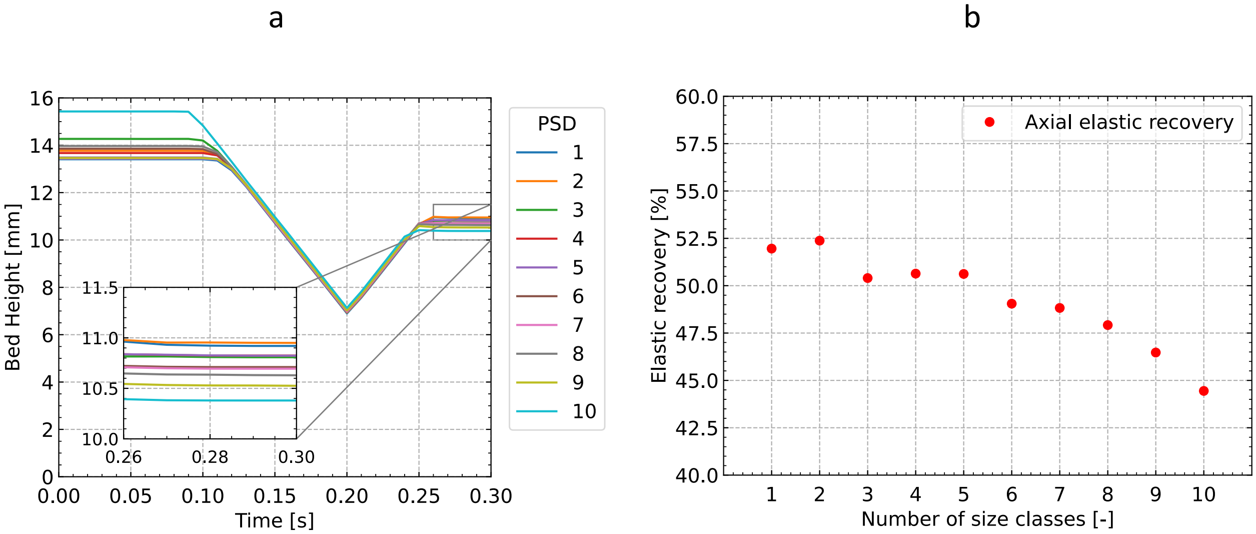

Fig. 11. Bed height and elastic recovery evolution for all ten PSDs: temporal evolution of bed height (a), elastic recovery of the final tablet (b).

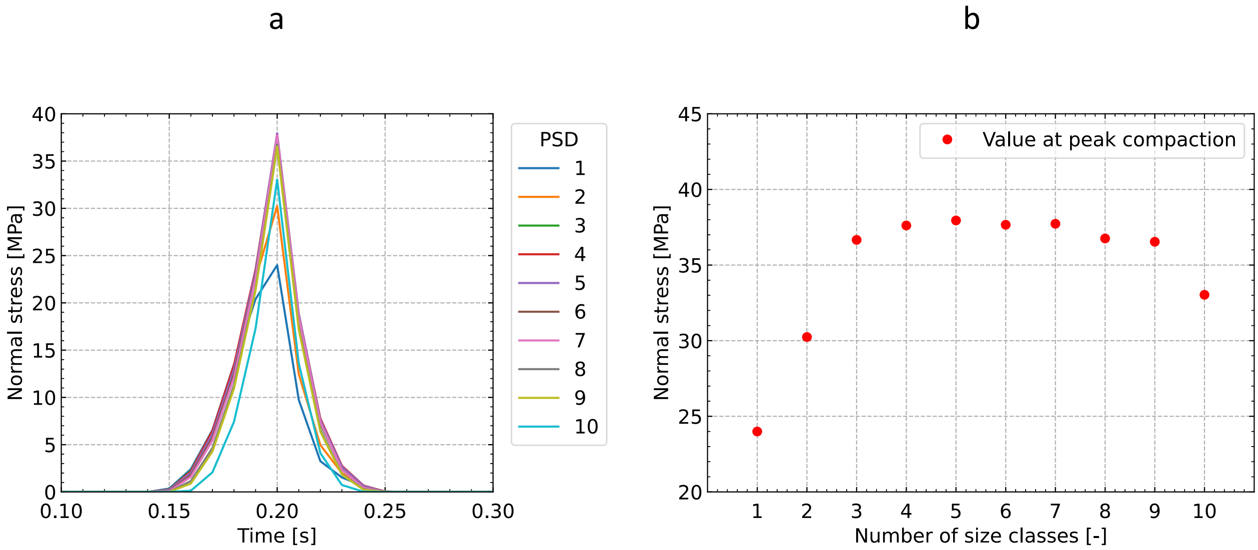

Fig. 12. Evolution of punch normal stress during compaction (a) and peak normal stress for all PSDs (b).

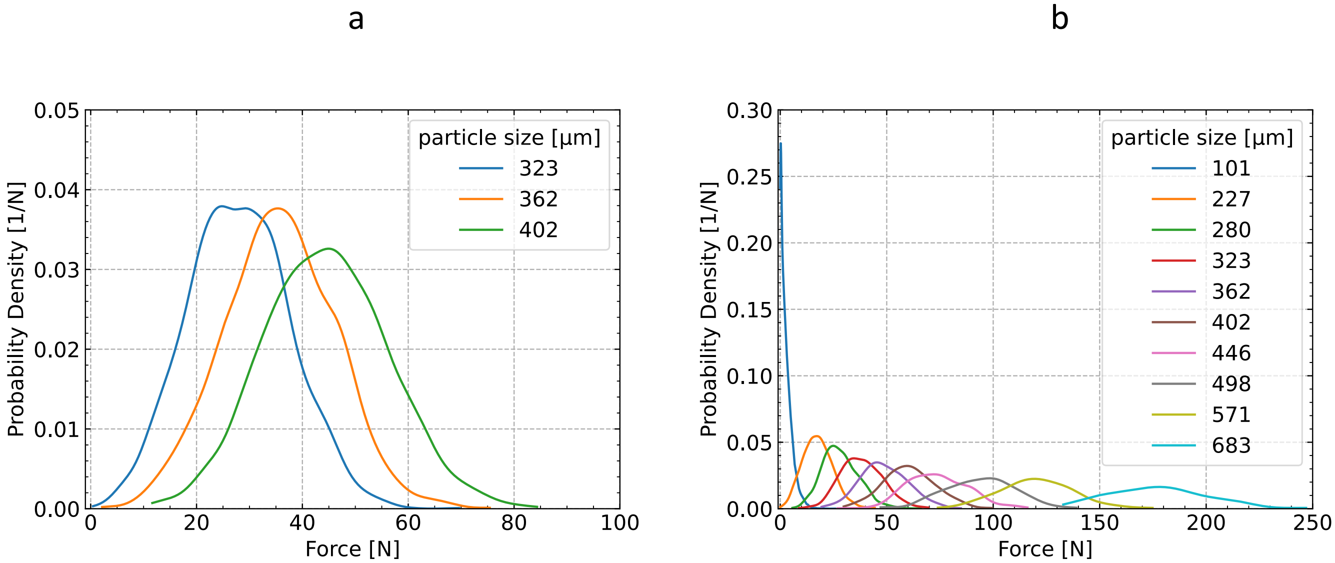

Fig. 13. Probability density function of force distribution across particle size classes: for simulation with three size classes PSD 3 (a) and ten size classes PSD 10 (b).

2.2. Simulation setup and calibration

The DEM simulations were carried out in EDEM 2022.1 (Altair Engineering Inc.). The virtual die geometry matched the experimental setup: a cylindrical die of radius 7 mm and height 15 mm Fig. 8. The upper punch followed the recorded STYL'One Evo displacement–time profile in Fig. 7, including its two characteristic velocity regimes: an initial motion at approximately 0.14 m/s until the punch reached the die rim, followed by a reduced velocity of 0.078 m/s during the main compaction phase of 100 ms. A dwell time of 1 ms was applied before unloading, matching the experimental cycle. The DEM timestep used in the simulations was 10^{-6} s. This value was determined automatically in EDEM for the Euler integration scheme. Using the exact kinematic profile is consistent with recent DEM-experiment integration practices that recommend applying real compaction trajectories to minimize boundary-condition artefacts [3,7].

For PSD 10, the system consisted of 26,632 particles after applying the uniform geometric scaling factor of three. Geometric scaling is commonly used in cohesive DEM to reduce computational cost, provided that contact parameters are calibrated for the scaled geometry. Recent studies have confirmed that adhesive elasto-plastic contact laws remain valid under moderate geometric scaling when effective stiffness and adhesion parameters are recalibrated appropriately [32,37,43].

Calibration was performed exclusively for PSD 10 and subsequently used unchanged for all PSDs and both contact models, ensuring that differences in compaction behaviour arise only from PSD and contact-law effects [27,28].

Calibration consisted of two steps:

1. Bulk-density matching

The particle density was adjusted until 1.23 g of powder produced a fill height of 15 mm after settling Fig. 9, matching the experimental die-fill density. This “effective density” technique is common when spherical particles are used in DEM, as it compensates for shape idealisation and ensures realistic packing behaviour [36,42].

2. Force-response matching

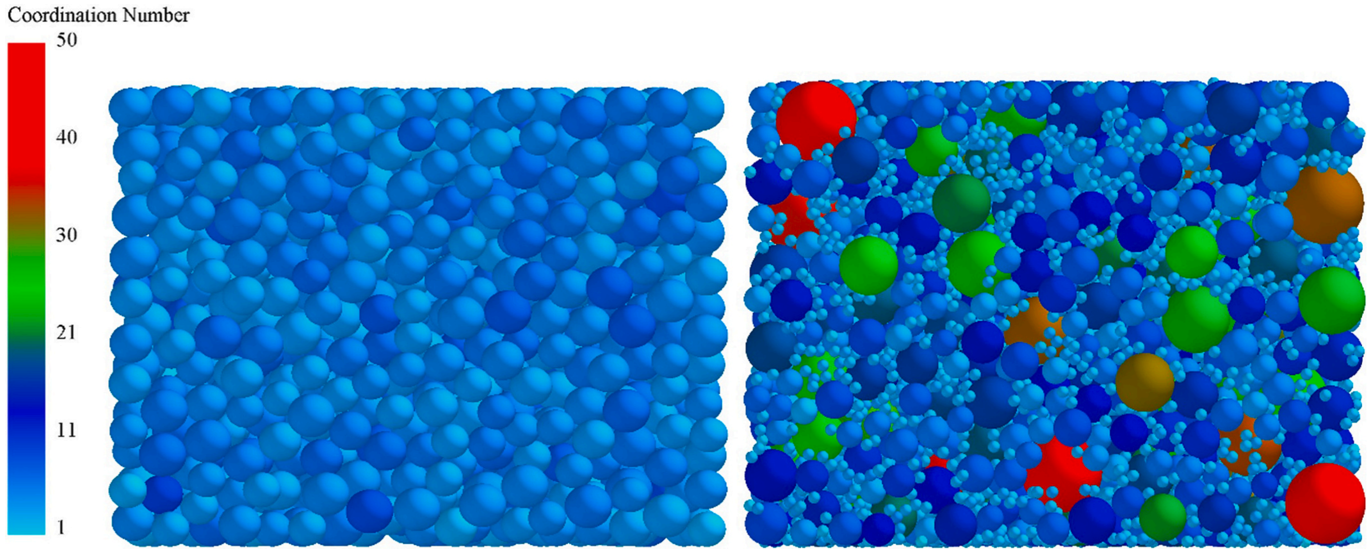

Fig. 14. Axial cross section of the tablet showing the coordination number across particle size classes after unloading: PSD 3 (a) and PSD 10 (b).

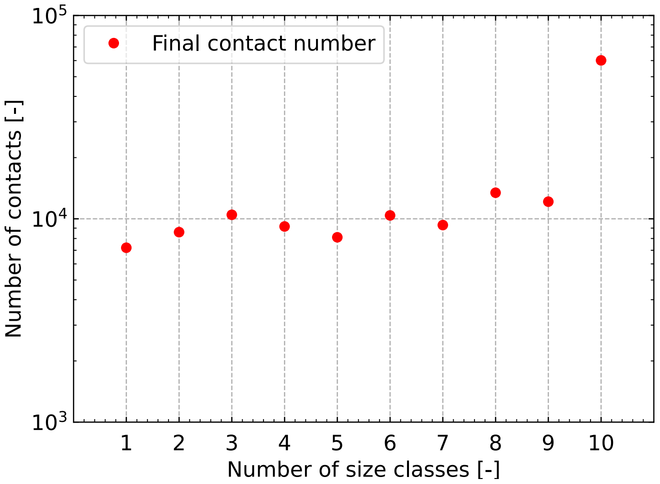

Fig. 15. Final total number of particle–particle contacts for PSD Classes 1–10.

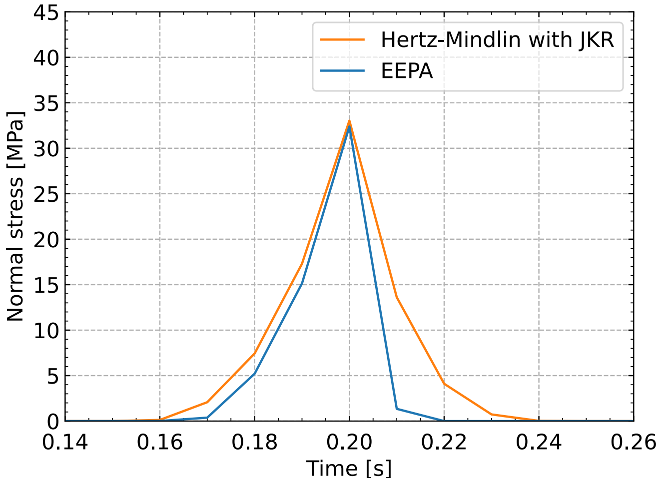

Fig. 17. Normal stress evolution for both the Hertz-Mindlin with JKR and EEPA models with PSD 10.

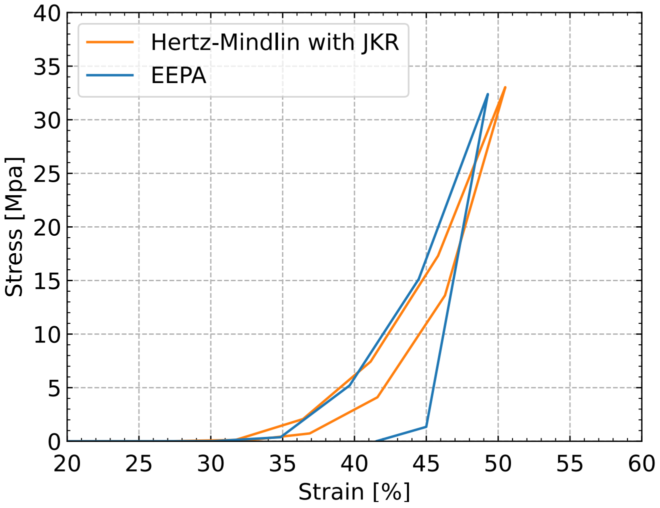

Fig. 16. Stress–strain responses for the Hertz-Mindlin with JKR and EEPA models with PSD 10.

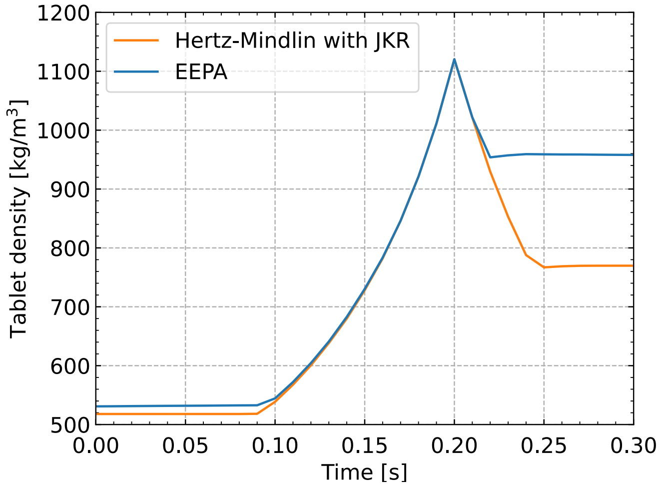

Fig. 18. Tablet density evolution for the Hertz-Mindlin with JKR and EEPA models with PSD 10.

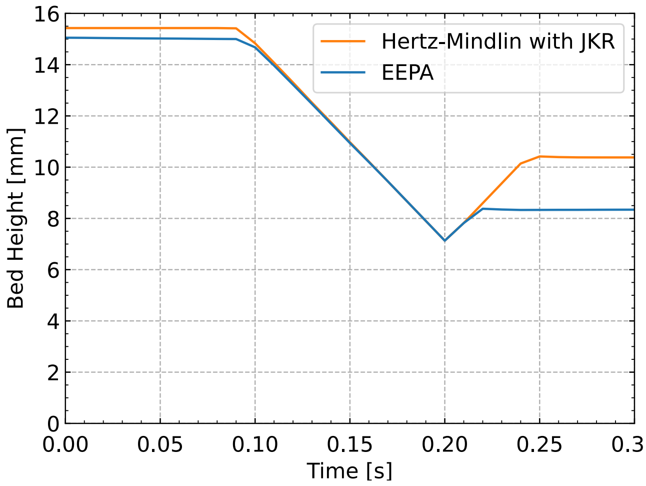

Fig. 19. Bed height evolution for both the Hertz-Mindlin with JKR and EEPA models with with PSD 10.

Contact parameters were tuned so that the imposed displacement profile generated a peak compaction force of approximately 5 kN, consistent with the STYL'One measurement Fig. 7. Cohesive DEM calibration does not yield a unique parameter set; instead, effective stiffness and adhesion parameters must be tuned to match macroscopic behaviour such as force–displacement curves [32,34,43].

After calibration, no parameters were modified. Consequently, variations in punch force, density evolution, elastic recovery, and contact-network structure across PSDs or contact models reflect physical changes rather than re-tuning effects. This single-calibration strategy aligns with modern DEM studies that analyse the mechanisms of PSD influence and contact-model behaviour under fixed material conditions [27,28].

2.3. *DEM models and simulations*

Two adhesive contact models were evaluated in this study: The Hertz–Mindlin model with Johnson–Kendall–Roberts (JKR) adhesion [44–46] and the Edinburgh Elasto–Plastic Adhesion (EEPA) model [47]. Both models are widely used for simulating cohesive particulate systems and are available in EDEM, where they enable the representation of normal and tangential contact forces, adhesion, and deformation processes relevant to powder compaction.

The Hertz–Mindlin model combines Hertzian elastic normal contact [45] with Mindlin's tangential contact formulation [44]. The JKR extension introduces an adhesive normal force based on surface energy considerations, allowing finite contact areas even at zero or slightly tensile loads [46]. This elastic–adhesive contact-law family has been applied extensively in DEM studies of cohesive powders, tablet formation and mechanical characterisation, although it is recognised that such models can overpredict elastic recovery for plastifying pharmaceutical materials [3,32].

The EEPA model incorporates both elastic and plastic components of deformation through a hysteretic loading–unloading path and an adhesive pull-off force [47]. This allows permanent deformation to accumulate during high-stress compaction and reduces the elastic recovery during unloading. Recent DEM studies have shown that elastoplastic adhesive formulations such as EEPA or its variants improve realism in simulating cohesive or amorphous powders, especially where irreversible densification and microstructural evolution are important [27,28,34].

The calibration procedure described in section 2.2 was first applied to the Hertz–Mindlin with JKR adhesion model using PSD 10. Once the force–displacement response showed satisfactory agreement with the experimental compaction curve, the same particle density, Young's modulus, Poisson's ratio, and punch kinematics were retained for the EEPA model. Only the EEPA-specific parameters were adjusted during its calibration [37], while all geometric and material inputs were kept unchanged Table 2. This approach is consistent with current recommendations that contact-model comparisons should be made under identical material and geometric conditions to isolate differences arising strictly from contact mechanics [32,43].

After calibration, no modifications were made to any model parameters. The PSD variation study (PSDs 1–10) was carried out exclusively with the Hertz–Mindlin–JKR model, while the comparison between contact models was performed only for PSD 10. This separation ensures that PSD effects and contact-model effects can be evaluated independently without parameter coupling or unintended calibration artefacts. Such separation of variables is increasingly emphasised in recent DEM compaction and microstructure-evolution studies [3,27,28].

Rolling resistance was not included in the present simulations in order to maintain a simplified and consistent contact framework across all cases and to focus the comparison on PSD breadth and normal contact law. This assumption may facilitate particle rotation and rearrangement, especially for irregular agglomerated particles, and may therefore affect the quantitative prediction of compaction behaviour. However, because the same assumption was applied to all simulated cases, the comparative trends reported here remain internally consistent.

3. Theory and calculation

The models used in this study, including the Hertz–Mindlin model with Johnson–Kendall–Roberts (JKR) adhesion and the Edinburgh Elasto–Plastic Adhesion (EEPA) model, are part of the EDEM software. Only essential theoretical elements are summarised here to clarify the differences in elastic, adhesive and plastic behaviour encoded in each model, which underlie the variations observed in the compaction simulations. Recent DEM literature has highlighted that the choice of contact model is often the dominant factor governing densification, elastic recovery and microstructural evolution in cohesive powders [3,28,32].

3.1. *Hertz-Mindlin model*

The Hertz–Mindlin model [44,45] assumes that particles interact as elastic spheres, with forces arising purely from elastic deformation. The normal contact force follows classical Hertzian contact mechanics:

$$F_n = \frac{4}{3} E^{*} \sqrt{R^{*}} \, \delta^{\frac{3}{2}} \tag{1}$$

Where:

- R^{*} = equivalent radius
- δ = normal overlap
- E^{*} = effective Young's modulus

The tangential force is calculated according to Mindlin's formulation:

Table 2
Calibrated parameters for the Hertz–Mindlin–JKR and EEPA contact models.

Simulation parameters	unit	Hertz-Mindlin with JKR	EEPA
Density	[kg/m^3]	1300	1300
Young's modulus	[GPa]	1	1
Poisson's ratio	[−]	0.25	0.25
Coefficient of restitution	[−]	0.6	0.6
Coefficient of static friction	[−]	0.5	0.5
Coefficient of rolling friction	[−]	0	0
Cohesion surface energy	[J/m^2]	1.5	1.5
Constant pull-off force	[N]	–	−0.0006
Contact plasticity ratio	[−]	–	0.9
Slope Exp	[−]	–	1
Tensile Exp	[−]	–	1
Tangential stiff multiplier	[−]	–	0.05

$$F_t = -S_t\,\delta_T \tag{2}$$

Where:

- δ_T = tangential overlap
- S_t = tangential stiffness

The Hertz–Mindlin model captures purely elastic behaviour. In cohesive powder compaction, this implies that the system stores a substantial amount of recoverable elastic energy. As shown in recent DEM studies, this model tends to overpredict elastic recovery and underpredict permanent deformation when applied to plastifying or amorphous materials [32,34].

3.2. Hertz-Mindlin model with JKR

The classical Hertz–Mindlin model is extended by the Johnson–Kendall–Roberts (JKR) formulation [46], which accounts for adhesive normal forces arising from surface energy. In the JKR model, the total normal force is:

$$F_{JKR} = -4\sqrt{\pi\,\gamma\,E^{*}}\,a^{\frac{3}{2}} + \frac{4\,E^{*}}{3\,R^{*}}\,a^{3} \tag{3}$$

Where:

- R^{*} = equivalent radius
- E^{*} = effective Young's modulus
- γ = surface energy
- a = contact radius.

The inclusion of JKR adhesion allows contacts to sustain a finite tensile force before separation. The Hertz–Mindlin–JKR formulation has been used widely in cohesive DEM studies of pharmaceutical powders, but it remains limited by its fully elastic unloading behaviour, which can exaggerate tensile contact retention and elastic rebound under unloading [3,28].

3.3. Edinburgh elasto-plastic adhesion (EEPA) model

The Edinburgh Elasto-Plastic Adhesion (EEPA) [47] introduces irreversible deformation through a hysteretic loading–unloading response.

The total normal contact force is:

$$F_n = F_{hys} + F_{nd} \tag{4}$$

where:

- F_{hys} = hysteretic spring force
- F_{nd} = normal damping force

The hysteretic spring force accounts for loading, unloading, and plastic deformation:

$$F_{hys} = \begin{cases} F_0 + k_1\,\delta^n \; if \; k_2\left(\delta^n - \delta_p^n\right) \ge k_1\,\delta^n \\ F_0 + k_2\left(\delta^n - \delta_p^n\right) \; if \; k_1\,\delta^n > k_2\left(\delta^n - \delta_p^n\right) > -k_{adh}\,\delta^n \\ F_0 - k_{adh}\,\delta^n \; if - k_{adh}\,\delta^n \ge k_2\left(\delta^n - \delta_p^n\right) \end{cases} \tag{5}$$

with:

- F_0 = constant adhesive strength at first contact
- k_1, k_2 and k_{adh} = loading, unloading and Adhesive stiffness parameters
- δ and δ_p = normal and plastic overlap
- n = non-linear index parameter

The normal damping force accounts for dissipation during particle separation:

$$F_{nd} = \beta_n \nu_n \tag{6}$$

with:

- ν_n = magnitude of the relative normal velocity
- β_n = normal dashpot coefficient

EEPA allows a portion of the deformation accumulated during loading to be plastic and non-recoverable, directly reducing elastic rebound during unloading. Recent studies have shown that elastoplastic adhesive contact models produce microstructural evolution and densification trends that align more closely with experimental behaviour for cohesive or amorphous excipients [27,28,34]. For these reasons, EEPA generally provides a more realistic representation of irreversible particle-scale deformation than purely elastic adhesive models in tableting simulations. Although additional parameter calibration could reduce differences between contact models for selected macroscopic observables, the remaining discrepancies in unloading behaviour, elastic recovery, and contact persistence also reflect intrinsic differences in the constitutive formulation of the models.

4. Results and discussion

The profiles and values reported in the following sections should be interpreted as qualitative and comparative indicators. The aim is to identify how variations in particle size distribution or contact models influence the underlying micromechanics of compaction, rather than to predict the exact numerical values of tablet properties.

4.1. Effect of particle size distribution on compaction behaviour using Hertz–Mindlin + JKR

In this part of the study, PSD Classes 1 to 10 shown in Fig. 3 and Table 1 were simulated using the Hertz–Mindlin contact model combined with Johnson–Kendall–Roberts (JKR) adhesion. PSD Class 1 corresponds to a monodisperse system, while PSD Class 10 represents the full discretized particle size distribution consisting of ten size classes.

4.1.1. Tablet density evolution

Fig. 10a presents the evolution of tablet density during compaction for PSD Classes 1 to 10 simulated with the Hertz Mindlin model and JKR adhesion. Density and porosity are inversely related, so only density is shown.

Before compression, broader PSDs begin with lower initial density. This effect is well established in granular packing theory. Fine particles can remain suspended in loose configurations and do not fully settle into available voids during gravitational filling, especially when cohesive or adhesive forces are present. This behaviour was described in classical work on PSD-controlled packing efficiency [48] and later confirmed for polydisperse sphere packings [49]. For cohesive systems, early DEM work showed that adhesion and assembly conditions strongly influence low density states and metastable structures [50]. More recent cohesive DEM calibration studies also report poor settling efficiency in adhesive powders due to cluster formation [32].

After compression, this trend reverses, as illustrated in Fig. 10. The narrowest PSDs reach the lowest final densities. For nearly monodisperse systems, the packing is geometrically inefficient and the rearrangement capacity is limited, so voids remain even at high stress. This behaviour is consistent with numerical studies where monodisperse or weakly polydisperse sphere packings show limited densification despite large applied loads [49]. In DEM simulations of pharmaceutical powder compaction, similar limitations in rearrangement and void closure have been reported when the microstructure lacks sufficient size contrast or shape diversity [31].

Intermediate PSDs achieve higher final densities than the narrow PSD, because extra size classes allow particles to occupy intermediate pore sizes and facilitate additional rearrangements. This is in line with work on bimodal and multimodal pharmaceutical mixtures, where the presence of appropriately chosen fine fractions improves packing, increases coordination number and leads to higher overall density at equivalent pressure [17,18].

The broadest PSDs reach the highest final densities as shown in Fig. 10b. In these systems, fine particles can migrate into residual voids during loading and effectively close pores that remain inaccessible in narrower PSDs. Microstructural characterisation of tablets by X-ray microtomography shows that fine particles and broad PSDs promote dense pore networks and higher solid fractions at a given compaction pressure [27,51,52]. Recent DEM and micromechanical studies on bimodal tablets confirm that fines enhance coordination number, alter force chains and support additional densification, especially at high relative densities [18,31].

A key factor underlying these trends is the strong coupling between PSD breadth and total particle count. The number of particles increases from 3470 in PSD Class 1 to 26,632 in PSD Class 10 as reported in Table 1. Similar behaviour has been reported in DEM studies of polydisperse and cohesive powders, where introducing fine particles increases both the number of contacts and the intensity of adhesion-mediated interactions [31,47,50]. In the present simulations, the larger population of fine particles in the broader PSDs results in a denser and more adhesive contact network, which suppresses elastic recovery during unloading and contributes directly to the higher final densities observed for these systems.

The density evolution across PSD Classes 1–10 reflects the combined influence of geometric packing, particle-count variations, and adhesion-driven contact stabilisation. Narrow PSDs, remain limited by poor void filling and restricted rearrangement. Intermediate PSDs benefit from improved packing due to additional size classes, while the broadest PSDs achieve the final densities because fine particles substantially increase the total number of adhesive contacts. These trends demonstrate that density evolution in the Hertz–Mindlin + JKR framework is governed primarily by PSD-induced changes in particle count and the resulting contact-network structure.

4.1.2. *Elastic recovery*

Fig. 11a shows the evolution of tablet height during compaction and unloading for PSD Classes 1–10, while Fig. 11b reports the resulting axial elastic recovery. Because the punch displacement profile is prescribed identically in all simulations, the bed height converges to similar minimum values at peak compression. Differences therefore arise primarily during unloading, where the internal contact network determines how strongly the compact expands once external loading is removed.

PSD classes with narrower distributions show the most pronounced elastic recovery. These systems contain fewer particles overall and therefore form fewer adhesive contacts under the Hertz–Mindlin + JKR model. With fewer stabilising interactions available, the compact experiences limited resistance to structural expansion upon punch retraction, resulting in comparatively larger bed-height rebound. Experimental observations for maltodextrin and related carbohydrate-based materials report similar behaviour, where tablets composed of coarser or more uniform particles undergo greater post-compression expansion due to reduced bond density [12,16].

PSD classes with intermediate breadth exhibit moderately reduced elastic recovery. As additional size classes are introduced, the number of particles and contacts increases, leading to a progressively stronger stabilising network during compression. Consequently, these systems show less rebound than the narrow PSDs but do not reach the low expansion levels of the broadest distributions.

The lowest elastic recovery is observed in PSD classes with broader distributions. These PSDs contain substantial fractions of fine particles, which markedly increase the total number of adhesive contacts formed during compaction Table 1. Adhesive DEM studies consistently report that systems with large fine-particle populations develop dense, highly interconnected contact networks that strongly constrain structural expansion during unloading [31,46,50]. The restrictive effect of this adhesive network is clearly reflected in the minimal rebound exhibited by the broadest PSDs in Fig. 11b, consistent with the high final densities reported in section 4.1.1.

Overall, the elastic recovery trends reflect PSD-dependent variations in particle count and contact-network density. Narrower PSDs exhibit substantial expansion after unloading due to limited adhesion, intermediate PSDs show a gradual reduction in rebound, and broader PSDs undergo minimal elastic recovery due to the extensive adhesive networks stabilising their compressed structures.

4.1.3. *Interparticle interaction*

The evolution of interparticle contact behaviour provides the link between the tablet-scale trends reported in sections 4.1.1 and 4.1.2 and the underlying micromechanics of compaction. Variations in PSD breadth modify the total number of particles present in the system and thereby alter the number, distribution, and strength of contacts formed during loading and unloading. These effects are consistent with observations for maltodextrin and other cohesive powders, where particle size strongly governs contact formation and bond density during compression [16]. Similar PSD-dependent changes in microstructure and interparticle connectivity have also been reported in experimental compaction studies [12]. In the present DEM simulations, the inclusion of adhesion via the Hertz–Mindlin + JKR model means that PSD-induced differences in particle count directly influence force transmission, coordination, and structural stability after unloading. The following subsections detail these mechanisms through the analysis of normal contact forces, contact number and connectivity, and their relationship to the macroscopic behaviour observed in earlier sections.

4.1.3.1. Normal stress and normal contact forces. Fig. 12a shows the evolution of normal stress experienced by the punch for PSD Classes 1–10, while Fig. 12b reports the corresponding peak values at maximum punch displacement. Because the compaction is displacement-controlled, all systems are compressed to the same global axial strain, but the resulting punch forces vary due to differences in packing and contact-network development. Narrow PSDs generate relatively low peak stresses because they contain fewer particles and therefore fewer load-bearing contacts. As additional size classes are introduced, the packing becomes mechanically stiffer: voids are filled more effectively, coordination increases Fig. 14, and the punch stress rises accordingly. This increase continues until approximately PSD Class 4–5, after which the peak stress enters a plateau region. For the broadest PSDs, especially Classes 9 and 10, the peak stress decreases again. This reduction reflects the fact that broader PSDs form highly dense and finely structured contact networks that offer multiple parallel low-force deformation paths under displacement-controlled loading, reducing the reaction force felt at the punch despite the higher final densities Fig. 10b. A similar interplay between packing structure and macroscopic stiffness in fine-rich cohesive systems has been reported in DEM studies [31,46,50].

The distribution of normal contact forces within the particle bed provides further insight into these trends. Fig. 13, which show the probability density functions of normal contact forces for a three-class PSD 3 Fig. 13a and the full ten-class PSD 10 Fig. 13b. In both cases, force transmission is strongly size-dependent: larger particles systematically experience higher individual force magnitudes, whereas fine particles experience many low-magnitude contacts. In PSD 3, this contrast is modest, with a limited range of force values and relatively small differences between size classes. In PSD 10, widening the distribution introduces much larger particles and many more fine particles, and the contrast becomes more evident: the largest particles carry the strongest forces in the system, while fine particles receive only very small forces. The role of fine particles is therefore not to bear significant load, but to increase the number of available low-force contacts that help distribute forces spatially. This behaviour aligns with previous analyses of multimodal granular packings, which report similar size-dependent differences in force magnitudes [48,49,53].

Fig. 14 shows the corresponding coordination number distributions for PSD 3 and PSD 10. Coordination number increases with particle size in both cases because larger particles have more geometric opportunities to form contacts. When the PSD is narrow Fig. 14a, the difference between large and small particles is limited: the largest particles reach coordination numbers of about 10–12, and the smallest particles form only 1–3 contacts. When the PSD is broadened Fig. 14b, these differences increase substantially. Introducing both larger particles and fine particles produces a more hierarchical contact structure: large particles form dozens of contacts, while fine particles remain weakly connected with only a few. Broadening the PSD therefore increases the overall connectivity of the system and sharpens the contrast in coordination number across particle sizes. These geometric effects are consistent with analyses of multimodal and polydisperse granular assemblies, where increasing PSD breadth leads to more complex and asymmetric contact networks [48,49,53].

Overall, the behaviour of the normal stress, normal contact forces, and coordination numbers is consistent across all PSDs. It should be noted, however, that the narrowest PSD cases also contain the fewest particles and contacts, which makes their stress response more sensitive to statistical variability associated with the limited size of the simulated system. The corresponding stress differences should therefore be interpreted primarily in a comparative and mechanistic sense rather than as exact quantitative predictions. These narrow PSDs also exhibit low macroscopic stiffness and relatively small force contrasts between particle sizes. As the PSD is broadened, both force magnitudes and coordination numbers diverge between large and small particles, with larger particles sustaining the highest forces and fine particles contributing primarily through numerous low-force contacts. In the broadest PSDs, the highly developed and finely interconnected contact network spreads the imposed load across many parallel interactions, reducing the peak stress felt by the punch while still enabling high final densities. These micromechanical observations link PSD breadth directly to the macroscopic behaviours described in sections 4.1.1 and 4.1.2.

4.1.3.2. Contact network topology and spatial organisation. Additional insight into the structural differences between PSDs is provided by the final total number of particle–particle contacts, shown in Fig. 15. Unlike coordination number, which describes the number of contacts per particle, the total contact number reflects the overall connectivity of the compact as a whole. Across PSD Classes 1–9, the final total number of contacts increases overall, following the broad trend expected from progressive PSD widening. Small oscillations appear between successive PSDs, which reflects the non-monotonic changes in particle count that arise from the way the distributions are constructed: widening the PSD alternately introduces larger and smaller classes, causing the total number of particles—and therefore the potential number of contacts—to fluctuate slightly from one PSD to the next. Despite these oscillations, PSD broadening between Classes 1–9 clearly increases the scale of the contact network.

PSD 10, however, remains distinct: because it contains by far the largest number of particles, it produces a final contact number that is roughly an order of magnitude higher than all other PSDs. This behaviour is consistent with findings in multimodal and polydisperse granular assemblies, where substantial increases in particle count and size diversity produce disproportionately dense contact networks [48,49,53] and with cohesive DEM results showing enhanced interconnectivity in fine-rich systems [31,46,50].

This highly connected network topology helps explain several macroscopic behaviours observed earlier. First, the dense network of available contact pathways in PSD Class 10 supports extensive load redistribution during compaction, which contributes to the reduction in peak punch stress reported in section 4.1.3.1. Second, the large number of small-force contacts stabilizes the tablet structure upon unloading, reducing elastic recovery as described in section 4.1.2. In contrast, the narrower PSDs form simpler and less redundant contact networks, which provide fewer alternative load paths and exhibit greater expansion during unloading.

Overall, the final contact-number results confirm that widening the PSD does more than modify per-particle coordination: it reorganises the entire particle assembly into a dense, multi-scale, highly interconnected structure. PSD Class 10 is distinct not only in the magnitude of its contact network but also in the qualitative organisation of that network, which underpins the macroscopic differences in densification, punch stress, and elastic recovery observed across the full set of PSDs.

4.2. Contact-model comparison with PSD 10

Before comparing the two contact models, it is important to recall that both simulations share the same geometric and material parameters described in section 2.2. Consequently, the differences reported in the following subsections arise from the intrinsic mechanics of the two contact models rather than from differences in base material properties or boundary conditions.

4.2.1. Normal stress: punch stress response

Fig. 16 compares the punch stress response predicted by the Hertz–Mindlin–JKR and EEPA contact models for the PSD 10 packing under the same displacement-controlled punch trajectory. Because the punch motion is prescribed, the stress–strain behaviour reflects how each contact model converts identical axial deformation into reaction forces.

Before the punch contacts the powder bed, the two simulations differ slightly in initial packing height, which affects only the time at which normal stress first appears. Once the punch reaches the bed surface, both systems follow the same imposed strain path during loading.

During compression, both contact models display a comparable rise in punch stress, and the loading branches nearly overlap Fig. 16. This similarity is expected because the two simulations share the same material and geometric parameters, and the EEPA-specific parameters were adjusted to reproduce the general macroscopic response under the same punch trajectory. As a result, both models provide similar effective stiffness in high-strain regimes [32,36].

After the peak strain is reached, the unloading behaviour shows clear differences between the two contact models. The EEPA curve drops rapidly, whereas the Hertz–Mindlin–JKR response decreases more gradually Fig. 16. A similar distinction is observed when examining the width of the normal stress over time Fig. 17. The EEPA stress signal begins slightly later in time due to the small difference in initial bed height, but the narrower overall stress–time profile is governed by the unloading behaviour itself: the EEPA curve loses stress more rapidly once the punch retracts, leading to a narrower overall stress–time profile. In contrast, the Hertz–Mindlin–JKR curve develops stress earlier and relaxes more slowly, producing a broader temporal response.

These differences stem from the intrinsic mechanics of the two contact models. The EEPA model incorporates elastoplastic deformation [47], so part of the deformation accumulated during loading is permanent, leaving comparatively little recoverable elastic energy once the punch retracts. This leads simultaneously to a steeper unloading slope in stress–strain space and a shorter unloading period in the stress–time curve. The Hertz–Mindlin–JKR formulation combines Hertzian elasticity with a tensile adhesive branch [46,50], allowing contacts to sustain small tensile forces and relax more gradually during unloading. This combination results in the smoother stress–strain decline and broader stress–time profile characteristic of the Hertz–Mindlin–JKR response.

4.2.2. Tablet density evolution

Fig. 18 shows the evolution of tablet density for the Hertz–Mindlin–JKR and EEPA contact models during compression and unloading of PSD 10. Before compression begins, the two cases exhibit slightly different initial densities. This is a direct consequence of their initial bed heights: approximately 15.5 mm for the Hertz–Mindlin–JKR case and around 15.0 mm for the EEPA case. This difference does not reflect any physical mechanism but simply shifts the point at which each powder bed makes contact with the descending punch.

Once the punch reaches the top of the powder bed, both systems experience the same imposed axial deformation. As a result, the density evolution during the entire loading phase is nearly identical for the two contact models. Both compact along the same trajectory and reach the same peak density at maximum compression. This is consistent with displacement-controlled compaction, where identical kinematics produce comparable macroscopic densification paths even when the underlying contact models differ [31,32,54].

The unloading phase reveals the primary distinction between the two models. In the EEPA simulation, tablet density decreases only slightly after the punch begins to retract, leading to a comparatively dense final compact. In contrast, the Hertz–Mindlin–JKR case shows a more pronounced density reduction during unloading, and the resulting tablet exhibits a lower final density. These differences mirror the trends observed in the stress–strain response in section 4.2.1, where the EEPA model showed a rapid stress decay and the Hertz–Mindlin–JKR model relaxed more gradually.

The underlying mechanisms responsible for these density changes arise from how each contact model handles the reversal of deformation. The EEPA formulation includes an elastoplastic loading–unloading response [47], meaning part of the particle overlap accumulated during compression is irreversible. When the punch retracts, only the elastic portion of the overlap is recovered, so the compact retains a substantial fraction of its deformation and stabilizes at a higher final density. This behaviour is consistent with DEM studies of plastifying cohesive powders, where limited elastic rebound leads to high residual packing densities after unloading [31,37].

In contrast, the Hertz–Mindlin–JKR model represents purely elastic deformation supplemented by an adhesive tensile branch [46,50]. During unloading, elastic forces tend to reopen contacts, and adhesion maintains cohesion only over a limited tensile range. As soon as the tensile capacity of a contact is exceeded, the overlap is fully released. This combination produces a more pronounced bulk expansion after peak compression and results in a lower final density. Similar behaviour has been reported in DEM studies of elastic–adhesive tablets, where reversible deformation and adhesive detachment during unloading lead to higher rebound and smaller final densities [50,55].

Overall, the density evolution highlights the fundamental mechanical distinction between the two contact models. Under identical compaction kinematics, both systems densify similarly during loading, but their unloading paths diverge: the elastoplastic EEPA model retains much of the compressed structure and yields a denser final compact, whereas the elastic–adhesive Hertz–Mindlin–JKR model undergoes greater structural relaxation and produces a less dense tablet.

4.2.3. Elastic recovery

Fig. 19 shows the bed-height evolution during unloading for the Hertz–Mindlin–JKR and EEPA contact models. After both systems reach the same peak compaction state, their responses diverge markedly once the punch begins to retract. The Hertz–Mindlin–JKR simulation exhibits a substantial rebound, with the bed height rising to approximately 10.5 mm, corresponding to an elastic recovery of about 45%. In contrast, the EEPA compact shows a much smaller rebound, stabilising at roughly 8.5 mm, or around 16% elastic recovery.

The origin of this difference follows directly from the unloading behaviour discussed in the previous section 4.2.2. Because the EEPA model incorporates an elastoplastic loading–unloading response, only a limited portion of the deformation accumulated during compression is recovered, which restricts volumetric rebound. The Hertz–Mindlin–JKR model, by contrast, represents fully reversible elastic deformation with an adhesive tensile branch [46,50], once the tensile capacity of the JKR adhesive branch is exceeded, contacts detach and the elastic overlap is fully released, which produces the larger rebound observed in the Hertz–Mindlin–JKR compact. As a result, the Hertz–Mindlin–JKR tablet undergoes a larger post-compaction height increase, while the EEPA compact retains most of its compressed structure.

4.2.4. Contact network and microstructure

The final contact structures obtained with the Hertz–Mindlin–JKR and EEPA models differ substantially, despite both simulations acting on the same PSD 10 particle configuration and undergoing identical compaction kinematics. These differences arise entirely from the unloading mechanics of the two contact models rather than from geometric or packing variations.

The Hertz–Mindlin–JKR model yields a post-compaction configuration with **60,136** particle–particle contacts. The network is cohesive but comparatively open, as many weak contacts detach during unloading. This reflects the reversible nature of the Hertzian elastic interaction and the limited tensile range of the JKR adhesive branch: once the adhesive limit is exceeded, contacts separate as the elastic overlap is released. As a result, the final structure exhibits pronounced load-bearing paths supported by a smaller number of weaker, non-persistent links [46,50,56].

The EEPA model produces a markedly more interconnected final configuration, with 77,680 contacts remaining after unloading. Because part of the deformation accumulated during loading is irreversible [47], a larger proportion of contacts remain closed once the elastic component is recovered. This leads to a denser contact structure that undergoes minimal rearrangement during the relaxation stage, a trend consistent with elastoplastic cohesive DEM models that retain more contact points after compaction [37,53].

The qualitative organisation of the contact structures further differentiates the two models. The Hertz–Mindlin–JKR configuration shows a clearer contrast between strong backbone contacts and peripheral weaker links, characteristic of elastic–adhesive microstructures where some contacts detach during unloading [50,56]. The EEPA configuration appears more homogeneous: medium-strength contacts remain widely distributed, and connectivity is maintained more uniformly across the compact due to the limited degree of contact reopening.

Ultimately, the contact configurations produced by the two models differ at the particle scale throughout the compaction process. The EEPA formulation generates a higher number of closed contacts both at peak load and after unloading because irreversible deformation limits the reopening of particle contacts. In contrast, the elastic–adhesive Hertz–Mindlin–JKR model forms fewer sustained contacts during loading and releases more of them during unloading as elastic overlap is recovered and adhesive limits are exceeded. As a result, the EEPA compact retains a denser and more uniformly connected contact structure, whereas the Hertz–Mindlin–JKR compact relaxes into a more open and less persistent network.

5. Conclusion

This study examined the influence of particle size distribution and contact-models on tablet compaction behaviour using DEM simulations. The PSD analysis showed that broader distributions lead to higher final densities, lower elastic recovery, and more interconnected microstructures due to increased contact opportunities and improved packing efficiency. These macroscopic trends were reflected at the particle scale through denser contact networks and more heterogeneous force transmission, particularly in multimodal configurations.

The comparison of the Hertz–Mindlin–JKR and EEPA contact models demonstrated that, under identical kinematics and material properties, the choice of contact model significantly affects unloading behaviour and the resulting tablet structure. While both models produced similar responses during loading, the elastoplastic EEPA formulation retained more of the imposed deformation, yielding higher final densities, reduced elastic recovery, and a more persistent and uniformly connected contact structure. In contrast, the elastic–adhesive Hertz–Mindlin–JKR model exhibited greater structural relaxation during unloading, resulting in lower final densities and fewer sustained contacts. These differences highlight the importance of contact-model selection when simulating cohesive powders, particularly when predicting post-compaction properties.

The DEM approach adopted here captures key qualitative mechanisms governing densification and microstructure development; however, several limitations remain. The simulations were conducted under idealised conditions with monodisperse material properties, rigid boundaries, and no fragmentation or particle deformation beyond the implemented contact models. Furthermore, only one PSD was used for the contact-model comparison, and the calibrated parameters reflect a single material and compaction setting. Future work could incorporate experimental validation, model parameter variability, and extended contact descriptions to further assess transferability across materials and loading conditions.

CRediT authorship contribution statement

Amine Ait Ouazzou: Writing – review & editing, Writing – original draft, Visualization, Validation, Project administration, Methodology, Investigation, Formal analysis, Data curation, Conceptualization. **Yogesh M. Harshe:** Writing – review & editing, Supervision, Project administration. **Vincent Meunier:** Writing – review & editing, Supervision. **Jan H. Finke:** Writing – review & editing, Supervision, Resources, Project administration. **Stefan Heinrich:** Writing – review & editing, Supervision, Software, Resources, Project administration, Funding acquisition, Conceptualization.

Declaration of competing interest

The authors declare that they have no known competing financial interests or personal relationships that could have appeared to influence the work reported in this paper.

Acknowledgement

This project has received funding from the European Union's Horizon 2020 research and innovation programme under the Marie Skłodowska-Curie grant agreement No 955661.

Data availability

Data will be made available on request.

References

[1] M. Saifullah, Y.A. Yusof, N.L. Chin, M.G. Aziz, M.A.P. Mohammed, N.A. Aziz, Tableting and dissolution characteristics of mixed fruit powder, Agric. Agric. Sci. Proc. 2 (2014) 18–25, https://doi.org/10.1016/J.AASPRO.2014.11.004.

[2] K. Koumbogle, R. Gosselin, F. Gitzhofer, N. Abatzoglou, Moisture behavior of pharmaceutical powder during the tableting process, Pharmaceutics 15 (2023), https://doi.org/10.3390/PHARMACEUTICS15061652/S1.

[3] Z. Li, H. Xiong, Q. Li, A. Naeem, L. Yang, W. Zhu, Y. Wu, Z. Jin, L. Ming, Advancements in the application of numerical simulation during tablet compaction, Pharmaceutics 17 (2025) 220, https://doi.org/10.3390/PHARMACEUTICS17020220.

[4] A. Russell, J. Strong, S. Garner, W. Ketterhagen, M. Long, M. Capece, Direct compaction drug product process modeling, AAPS PharmSciTech 23 (1) (2022) 67, https://doi.org/10.1208/S12249-021-02206-4.

[5] M. Sohail Arshad, S. Zafar, B. Yousef, Y. Alyassin, R. Ali, A. AlAsiri, M.W. Chang, Z. Ahmad, A. Ali Elkordy, A. Faheem, K. Pitt, A review of emerging technologies enabling improved solid oral dosage form manufacturing and processing, Adv. Drug Deliv. Rev. 178 (2021), https://doi.org/10.1016/J.ADDR.2021.113840.

[6] S.S. Gaikwad, S.J. Kshirsagar, Review on tablet in tablet techniques, beni. Suef. Univ. J. Basic Appl. Sci. 9 (2020) 1–7, https://doi.org/10.1186/S43088-019-0027-7/FIGURES/3.

[7] R. Rösemeier-Scheumann, L. Wagner, U. Bobe, A. Bozon, A. Kwade, J.H. Finke, Structural and functional analysis of a new co-processed tableting excipient for food compaction processes, J. Food Eng. 363 (2024) 111624, https://doi.org/10.1016/J.JFOODENG.2023.111624.

[8] N.L. Martin, A.K. Schomberg, J.H. Finke, T.G.M. Abraham, A. Kwade, C. Herrmann, Process modeling and simulation of tableting—an agent-based simulation methodology for direct compression, Pharmaceutics 13 (2021), https://doi.org/10.3390/PHARMACEUTICS13070996.

[9] P.H.M. Janssen, S. Fathollahi, B. Bekaert, D. Vanderroost, T. Roelofs, V. Vanhoorne, C. Vervaet, B.H.J. Dickhoff, Impact of material properties and process parameters on tablet quality in a continuous direct compression line, Powder Technol. 424 (2023) 118520, https://doi.org/10.1016/J.POWTEC.2023.118520.

[10] I.C. Sinka, F. Motazedian, A.C.F. Cocks, K.G. Pitt, The effect of processing parameters on pharmaceutical tablet properties, Powder Technol. 189 (2009) 276–284.

[11] L.X. Yu, G. Amidon, M.A. Khan, S.W. Hoag, J. Polli, G.K. Raju, J. Woodcock, Understanding pharmaceutical quality by design, AAPS J. 16 (2014) 771, https://doi.org/10.1208/S12248-014-9598-3.

[12] F. Fichtner, Å. Rasmuson, G. Alderborn, Particle size distribution and evolution in tablet structure during and after compaction, Int. J. Pharm. 292 (2005) 211–225, https://doi.org/10.1016/J.IJPHARM.2004.12.003.

[13] Y. Wang, J. Cao, X. Zhao, Z. Liang, Y. Qiao, G. Luo, B. Xu, Using a material library to understand the change of tabletability by high shear wet granulation, Pharmaceutics 14 (2022) 2631, https://doi.org/10.3390/PHARMACEUTICS14122631/S1.

[14] S. Virtanen, O. Antikainen, H. Räikkönen, J. Yliruusi, Granule size distribution of tablets, J. Pharm. Sci. 99 (2010) 2061–2069, https://doi.org/10.1002/JPS.21945.

[15] A. Kuriyama, Y. Ozaki, Assessment of active pharmaceutical ingredient particle size in tablets by raman chemical imaging validated using polystyrene microsphere size standards, AAPS PharmSciTech 15 (2014) 375, https://doi.org/10.1208/S12249-013-0064-9.

[16] I. Wünsch, J.H. Finke, E. John, M. Juhnke, A. Kwade, The influence of particle size on the application of compression and compaction models for tableting, Int. J. Pharm. 599 (2021), https://doi.org/10.1016/j.ijpharm.2021.120424.

[17] S.M. Razavi, M. Gonzalez, A.M. Cuitiño, Quantification of lubrication and particle size distribution effects on tensile strength and stiffness of tablets, Powder Technol. 336 (2018) 360–374, https://doi.org/10.1016/j.powtec.2018.06.001.

[18] M. Zhao, A. Luo, Y. Zhou, Z. Liu, Y. Wang, L. Luo, Y. Jiang, J. Tang, Z. Lu, T. Guan, L. Chen, H. Sun, C. Dai, Evolution characteristics of micromechanics provides insights into the microstructure of pharmaceutical tablets fabricated by bimodal mixtures, Sci. Rep. 13 (2023) 20247, https://doi.org/10.1038/S41598-023-47239-W.

[19] Y. Kudo, M. Yasuda, S. Matsusaka, Effect of particle size distribution on flowability of granulated lactose, Adv. Powder Technol. 31 (2020) 121–127, https://doi.org/10.1016/J.APT.2019.10.004.

[20] A. Parikh, S. Agarwal, K. Raut, A Review on Applications of Maltodextrin in Pharmaceutical Industry. https://api.semanticscholar.org/CorpusID:15249552, 2014 (accessed November 10, 2023).

[21] A. Kucharska-Guzik, Ł. Guzik, A. Charzyńska, A. Michalska-Ciechanowska, Influence of freeze drying and spray drying on the physical and chemical properties of powders from *Cistus creticus* L. Extract Foods 14 (2025) 849 https://doi.org/10.3390/FOODS14050849/S1.

[22] M.T.L. Pereira, M.P. Cavalcante, S.F. da Silva, Y. Sensheng, S. dos S. Silva, A.C. de Aquino, Í.M. da S. Araújo, E.S. Dantas, B.M.B. da Silva, E. de G. Alves Filho, L.M.A. e. Silva, S.V. Frota Gaban, Effect of different carrier agents on the yield of powered plant beverage obtained by spray drying and characterization of physicochemical properties, ACS Food Sci. Technol. 4 (2024) 2392–2399, https://doi.org/10.1021/ACSFOODSCITECH.4C00478.

[23] T. Ojsteršek, G. Hudovornik, F. Vrečer, Comparative study of selected excipients influence on carvedilol release from hypromellose matrix tablets, Pharmaceutics 15 (2023) 1525, https://doi.org/10.3390/PHARMACEUTICS15051525/S1.

[24] Z. Saavedra-Leos, C. Leyva-Porras, S.B. Araujo-Díaz, A. Toxqui-Terán, A.J. Borrás-Enríquez, Technological application of maltodextrins according to the degree of polymerization, Molecules 20 (2015) 21067–21081, https://doi.org/10.3390/MOLECULES201219746.

[25] P. Cleary, Discrete element modelling of industrial granular flow applications, TASK Q. 2 (1998) 385–415.

[26] S. Rajendran, T.R. Vakamalla, N. Mangadoddy, Numerical methods in mineral processing: an overview, in: Mineral Processing: Beneficiation Operations and Process Optimization through Modeling, 2023, pp. 251–285, https://doi.org/10.1016/B978-0-12-823149-4.00012-0.

[27] M. Soundaranathan, M. Al-Sharabi, T. Sweijen, P. Bawuah, J.A. Zeitler, S. Majid Hassanizadeh, K. Pitt, B.F. Johnston, D. Markl, Modelling the evolution of pore structure during the disintegration of pharmaceutical tablets, Pharmaceutics (2023), https://doi.org/10.3390/pharmaceutics15020489.

[28] A.-S. Persson, J. Nordström, K. Giannis, A. Kwade, J.H. Finke, C. Schilde, The effect of particle shape on the compaction of realistic non-spherical particles-a multi-contact DEM study, Pharmaceutics (2023), https://doi.org/10.3390/pharmaceutics15030909.

[29] W. Zunker, S. Dunatunga, S. Thakur, P. Tang, K. Kamrin, Experimentally validated DEM for large deformation powder compaction: mechanically-derived contact

model and screening of non-physical contacts, Powder Technol. 459 (2025) 120972, https://doi.org/10.1016/J.POWTEC.2025.120972.

[30] A. Rogers, M. Ierapetritou, Challenges and opportunities in pharmaceutical manufacturing modeling and optimization, Comp. Aided Chem. Eng. 34 (2014) 144–149, https://doi.org/10.1016/B978-0-444-63433-7.50015-8.

[31] K. Giannis, C. Schilde, J.H. Finke, A. Kwade, Modeling of high-density compaction of pharmaceutical tablets using multi-contact discrete element method, Pharmaceutics 13 (2021), https://doi.org/10.3390/PHARMACEUTICS13122194.

[32] C.J. Coetzee, O.C. Scheffler, Review: the calibration of DEM parameters for the bulk modelling of cohesive materials, Processes 2023 11 (2022) 5, https://doi.org/10.3390/pr11010005.

[33] S. Bin Yeom, E. Ha, M. Kim, S.H. Jeong, S.J. Hwang, D.H. Choi, Application of the discrete element method for manufacturing process simulation in the pharmaceutical industry, Pharmaceutics 11 (2019), https://doi.org/10.3390/PHARMACEUTICS11080414.

[34] W. Nan, W.P. Goh, M.T. Rahman, Elasto-plastic and adhesive contact: an improved linear model and its application, Powder Technol. 407 (2022), https://doi.org/10.1016/j.powtec.2022.117634.

[35] R. Almutairi, A.R. Basson, P. Wearsh, F. Cominelli, A. Rodriguez-Palacios, Validity of food additive maltodextrin as placebo and effects on human gut physiology: systematic review of placebo-controlled clinical trials, Eur. J. Nutr. 61 (2022) 2853, https://doi.org/10.1007/S00394-022-02802-5.

[36] M. Marigo, E.H. Stitt, Discrete element method (DEM) for industrial applications: comments on calibration and validation for the modelling of cylindrical pellets, KONA Powder Part. J. (2015) 236–252, https://doi.org/10.14356/kona.2015016.

[37] M.J. Mohajeri, R.L.J. Helmons, C. van Rhee, D.L. Schott, A hybrid particle-geometric scaling approach for elasto-plastic adhesive DEM contact models, Powder Technol. 369 (2020) 72–87.

[38] A.A. Ouazzou, Y.M. Harshe, V. Meunier, J.H. Finke, S. Heinrich, Influence of process parameters and particle size distribution on mechanical properties of tablets, Chem. Ing. Tech. 95 (2023) 168–177, https://doi.org/10.1002/CITE.202200157.

[39] K.R. Shull, Contact mechanics and the adhesion of soft solids, Mater. Sci. Eng. R. Rep. 36 (2002) 1–45.

[40] A.S. Mijailovic, B. Qing, D. Fortunato, K.J. Van Vliet, Characterizing viscoelastic mechanical properties of highly compliant polymers and biological tissues using impact indentation, Acta Biomater. 71 (2018) 388–397, https://doi.org/10.1016/J.ACTBIO.2018.02.017.

[41] L. Wan, F. Lin, Research on material viscoelasticity and its influence on indentation rolling resistance, Applied Sciences 2024, Vol. 14, Page 3750, Appl. Sci. 14 (2024) 3750, https://doi.org/10.3390/APP14093750.

[42] B. Jadidi, M. Ebrahimi, F. Ein-Mozaffari, A. Lohi, Calibration of DEM input parameters for simulation of the cohesive materials: comparison of response surface method and machine learning models, Particuology 100 (2025) 214–231, https://doi.org/10.1016/J.PARTIC.2025.03.018.

[43] J. Diviš, D. Žurovec, Á. Ramírez-Gómez, J. Hlosta, J. Rozbroj, K. Pokorná, J. Nečas, J. Zegzulka, DEM calibration insights on the role of particle shape for sub 2 mm particles, Sci. Rep. 15 (1) (2025) 20477-, https://doi.org/10.1038/s41598-025-04592-2.

[44] R.D. Mindlin, Compliance of elastic bodies in contact, J. Appl. Mech. 16 (1949) 259–268, https://doi.org/10.1115/1.4009973.

[45] H. Hertz, On the contact of elastic solids, J. Reine Angew. Math. 92 (1882) 156–171.

[46] K.L. Johnson, et al., Surface energy and the contact of elastic solids, Proc. R. Soc. Lond. A. Math. Phys. Sci. 324 (1971), https://doi.org/10.1098/rspa.1971.0141.

[47] S.C. Thakur, Others, micromechanical analysis of cohesive granular materials using the discrete element method with an adhesive elasto-plastic contact model, Granul. Matter 16 (2014) 383–400, https://doi.org/10.1007/s10035-014-0506-4.

[48] H.Y. Sohn, C. Moreland, The effect of particle size distribution on packing density, Can. J. Chem. Eng. 46 (1968) 162–167.

[49] K.W. Desmond, E.R. Weeks, Influence of particle size distribution on random close packing of spheres, Phys. Rev. E 90 (2014) 22204.

[50] F. Gilabert, et al., Computer simulation of model cohesive powders: influence of assembling procedure and contact laws on low consolidation states, Phys. Rev. E 75 (2007).

[51] A.K. Schomberg, A. Diener, I. Wünsch, J.H. Finke, A. Kwade, The use of x-ray microtomography to investigate the microstructure of pharmaceutical tablets: potentials and comparison to common physical methods, Int. J. Pharm. X 3 (2021), https://doi.org/10.1016/j.ijpx.2021.100090.

[52] D. Markl, A. Strobel, R. Schlossnikl, J. Bøtker, P. Bawuah, C. Ridgway, J. Rantanen, T. Rades, P. Gane, K.E. Peiponen, J.A. Zeitler, Characterisation of pore structures of pharmaceutical tablets: a review, Int. J. Pharm. 538 (2018) 188–214, https://doi.org/10.1016/J.IJPHARM.2018.01.017.

[53] J. Wiacek, M. Stasiak, J. Kafashan, Structural and micromechanical properties of ternary granular packings: effect of particle size ratio and number fraction of particle size classes, Materials 13 (2020) 339.

[54] Y. Hayashi, Y. Marumo, T. Takahashi, Y. Nakano, A. Kosugi, S. Kumada, D. Hirai, K. Takayama, Y. Onuki, In silico predictions of tablet density using a quantitative structure-property relationship model, Int. J. Pharm. 558 (2019) 351–356, https://doi.org/10.1016/J.IJPHARM.2018.12.087.

[55] S. van den Ban, D.J. Goodwin, The impact of granule density on tabletting and pharmaceutical product performance, Pharm. Res. 34 (2017) 1002–1011, https://doi.org/10.1007/S11095-017-2115-5.

[56] O. Baran, Others, DEM simulation of a schulze ring shear tester, AIP Conf. Proc. 1145 (2009), https://doi.org/10.1063/1.3179948.